

Solute Segregation Activates Unconventional Grain Boundary Disconnections

Zuoyong Zhang and Chuang Deng*

Department of Mechanical Engineering, University of Manitoba, Winnipeg, Manitoba R3T 5V6, Canada

*Corresponding author: chuang.deng@umanitoba.ca

Abstract

Disconnections, now recognized as key mediators of grain boundary (GB) kinetics in polycrystals, have traditionally been associated with thermal or mechanical activation. Here, using atomistic simulations across multiple binary alloys (Al-Ni, Al-Fe, etc.), we reveal a distinct disconnection formation mechanism solely activated by interstitial solute segregation. This process exhibits a zero-nucleation energy barrier, contrasting sharply with conventional disconnection nucleation. We identify two segregation-induced disconnection types: (I) annihilable disconnections that promote GB migration and annihilate with continued segregation, and (II) permanent disconnections with stable dipoles that resist shear, inducing GB amorphization and sliding rather than conventional shear-coupled motion. The permanent disconnections generate localized stress fields that further drive solute accumulation and, at higher concentrations, facilitate precipitation. These disconnections, unprecedented in pure systems, follow unique nucleation pathways as confirmed by dichromatic pattern analysis and persist across diverse crystal structures. This work establishes solute segregation as a route for barrier-free disconnection formation, fundamentally altering our understanding of GB kinetics in alloys.

Grain boundaries (GBs) and their kinetics play a crucial role in the microstructural evolution and physical properties of polycrystalline materials. In recent years, a unified theoretical framework based on disconnections has emerged, positioning disconnections as the fundamental defects governing GB kinetics [1]. GB disconnections are topological defects confined to GBs that possess both step and dislocation character [2–4]. In general, the step component governs the normal GB motion, while the dislocation character drives simultaneous shear displacements of grains, giving rise to shear-coupled GB migration in polycrystalline materials [1,5–8].

According to the disconnection theorem [1], GB migration involves two distinct processes: nucleation and subsequent migration of disconnections. The nucleation of a disconnection dipole requires overcoming a substantial activation energy barrier, typically through thermal or mechanical loading [5].

Once nucleated, the disconnection dipole can migrate by overcoming a much lower energy barrier [6]. In pristine materials, where nucleation occurs homogeneously, the overall kinetics of GB migration are generally limited by this nucleation process [9]. For a given GB structure, it is theoretically possible to enumerate all disconnection modes based on its dichromatic pattern [1]. This, in turn, enables the derivation of energy barriers and the prediction of GB kinetics. The disconnection theorem thus offers a powerful framework for linking GB structure to migration behavior, a longstanding challenge due to the complexity of the five-dimensional GB parameter space, despite over a century of research [10,11].

Beyond facilitating GB migration, disconnection motion also governs a range of other GB kinetic processes, including grain rotation [12–15], GB curvature evolution and roughening [1,16,17], and topological phase transitions at GBs [18]. While most studies on disconnection-mediated GB kinetics have focused on pure systems, impurity segregation introduces an additional mechanism for regulating GB kinetics, enabling phenomena such as segregation-induced GB phase transitions [19–21], diffusion-induced GB migration [22], and GB stabilization [23,24]. Recent studies have reported that pre-existing disconnections at twin boundaries can alter the solute segregation pattern due to the changes in local symmetry [25]. At low solute concentrations, disconnection dipoles tend to annihilate, whereas higher concentrations can stabilize these dipoles through solute clustering at disconnection cores [26]. However, these investigations primarily examine segregation effects on twin boundary kinetics in systems where disconnections are manually introduced. The role of solute segregation in the formation of GB disconnections, and its broader implications for GB kinetics, remains largely unexplored.

In this letter, we report a solute segregation–activated mechanism for disconnection formation that exhibits a zero-nucleation energy barrier, as revealed by atomistic simulations. Unlike conventional disconnections, which are highly mobile and facilitate shear-coupled GB migration in pure systems, the segregation-activated disconnections are effectively immobile under shear and instead result in GB sliding. As the solute concentration increases further, stress fields associated with the stationary disconnection cores promote localized precipitation.

FIG. 1 demonstrates the nucleation and evolution of two types of disconnections due to the interstitial segregation in a representative substitutional binary alloy system, Al-Ni: type I (annihilable) and type II (permanent). After hybrid molecular dynamics (MD)/Monte Carlo (MC) simulations detailed in Supplementary Materials (SM) [27] (see also Refs. [28–40] therein), Ni atoms were found to segregate to interstitial sites within the kite structures of the Al $\Sigma 5(210)$ symmetric tilt GB (STGB), consistent with

previous observations [41] and additional first-principles simulations based on the density functional theory (see SM [27]). At low global solute concentrations (e.g., $X_{Ni}^{global} < 0.67$ at.%), the STGB tends to separate into two distinct regions: (i) segregation zone, where Ni atoms occupy interstitial sites, and (ii) none-segregation zone (region ②), which remains free of solute atoms, as shown in FIG. 1(a). Notably, a disconnection dipole emerges at the joints between these two regions, as highlighted by the light blue arrows in FIG. 1(a).

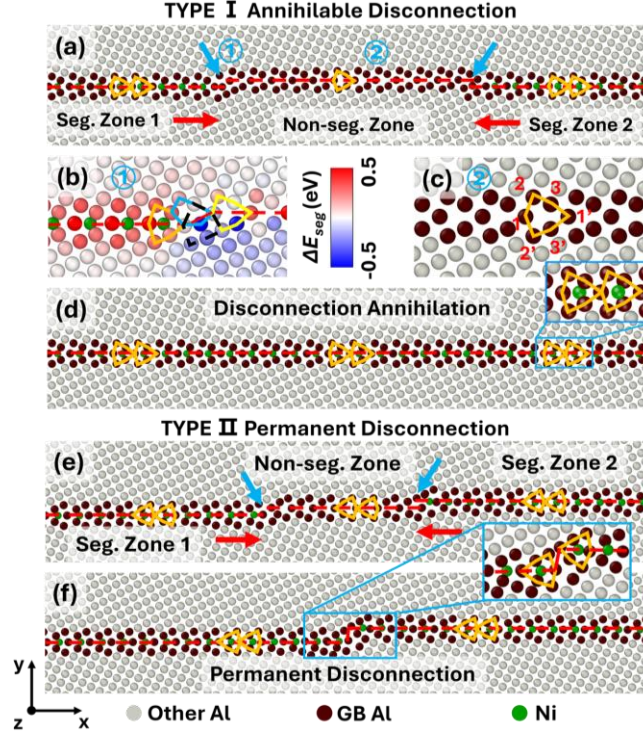


FIG. 1 Two types of disconnections observed in the $\Sigma 5(210)$ STGB after hybrid MD/MC simulations at 300 K in the Al-Ni system. (a) Nucleation of a type I annihilable disconnection dipole at low solute concentration ($X_{Ni}^{global} < 0.67$ at.%). (b) Segregation energy ΔE_{seg} map of Ni in Ag at a disconnection. (c) Atomic configuration at the non-segregated GB region ②. (d) Disconnection annihilation at higher solute concentration ($X_{Ni}^{global} \geq 0.67$ at. %). (e) Nucleation of a type II permanent disconnection at low global Ni concentration. (f) Continuous interstitial segregation of Ni atoms finally forms a permanent disconnection. The insets in (d) and (f) are used to highlight the interstitial segregation and permanent disconnection, respectively.

This interstitial segregation resembles the previously reported segregation-induced filled-kite transition [19]. In that context, the disconnections in FIG. 1(a) could be interpreted as a type of phase junctions [42]. However, a key distinction lies in the activation mechanism: the filled-kite transition requires thermal activation to overcome a finite energy barrier. It is crucial to note that the observed interstitial segregation did not result from atom insertion or deletion, but rather from initial substitution followed by GB evolution and relaxation. This process is driven by the significant reduction in GB excess

energy resulting from interstitial solute segregation, even though the formation of disconnections contributes negatively to this energy reduction (FIG. S2 [27]). This energetic balance explains why these unconventional disconnections can nucleate without any energy barrier. First-principles simulations in the Al-Ni and Al-Fe systems further confirm that once solute atoms occupy the 3 or 3' sites as shown in FIG. 1(c), they preferentially drive the migration of GB kite structures either upward or downward. This solute-induced GB evolution ultimately results in the formation of a disconnection (FIG. S3 [27]), in agreement with the disconnection nucleation paths obtained from dichromatic pattern analysis shown in FIG. 2. Therefore, we refer to this behavior as GB interstitial segregation [41], and the resulting discontinuities as GB disconnections.

The disconnection dipole can be annihilated by increasing the solute concentration beyond 0.67 at.%, a threshold determined by the ratio of available interstitial sites within the two GBs of the Al bicrystal. The annihilation of such dipole results in an interstitially segregated flat GB, as shown in FIG. 1(d), driven by the continuous segregation of Ni atoms. FIG. 1(b) presents the segregation energy maps of Ni atoms around the disconnection ① in FIG. 1(a). The segregated region exhibits a standard kite structure (orange), which connects to a highly distorted unsegregated kite (light blue), followed by a slightly distorted unsegregated kite (yellow). The map indicates that Ni atoms preferentially segregate to site 3' (as illustrated in FIG. 1(c)) within the light blue kite, which has the lowest segregation energy among all sites surrounding disconnection ①. Upon segregation, the dark-dashed kite transforms into a standard segregated kite, like the orange one to its left, through GB relaxation. This transformation subsequently distorts the adjacent yellow kite, initiating a sequential process. A similar evolution occurs at the opposite disconnection of the dipole. Consequently, the overall segregation-induced annihilation follows the direction of the red arrows in FIG. 1(a), ultimately producing a flat GB in FIG. 1(d). Moreover, this interstitial segregation and dipole annihilation can induce GB migration downward. Due to the symmetry of the GB structure, upward GB migration may also occur if Ni atoms simultaneously segregate to site 3 at different regions of the GB.

Another scenario arises when solute atoms simultaneously segregate to sites 3 and 3' in the same GB. This leads to the formation of a disconnection “embryo”, as illustrated in FIG. 1(e). Segregation to the upper sites (site 3) induces upward GB migration (Seg. Zone 2 in FIG. 1(e)), while segregation to the lower sites (site 3') drives downward GB migration (Seg. Zone 1). The region between these two zones remains non-segregated, retaining the original kite structures characteristic of the pure system. The disconnections at the boundaries between these regions, marked by light blue arrows in Fig. 1(e),

resemble the annihilable dipoles shown in FIG. 1(a). However, in contrast to the earlier case, further interstitial segregation drives the motion of these disconnections without leading to their annihilation. Instead, they merge to form a stable, permanent disconnection, as shown in FIG. 1(f). For clarity, only a single permanent disconnection is shown here. Due to periodic boundary conditions, a corresponding opposite disconnection must exist elsewhere along the same GB.

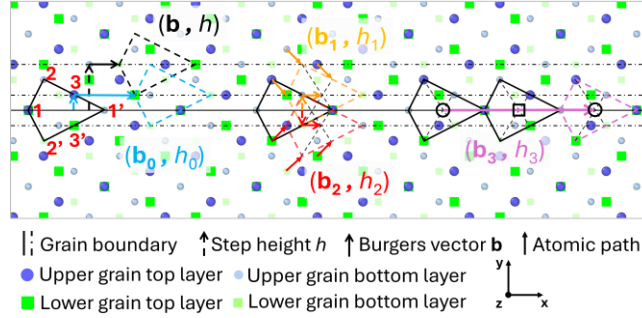


FIG. 2 Dichromatic pattern comparison between conventional [5,30] and segregation-induced disconnections in the $\Sigma 5(210)$ STGB of an Al bicrystal. The black solid kites represent the original kite structures, while the dashed kites are new kites after nucleation.

As established, the disconnections studied here differ fundamentally from conventional disconnections in their formation mechanisms. Accordingly, their nucleation pathways also diverge. In FIG. 2, the black step height h and Burgers vector \mathbf{b} represent the nucleation path of a conventional disconnection widely reported in the pristine Cu $\Sigma 5(210)$ STGB, characterized by a shear-coupling factor $\beta = b/h = 2/3$ [5,43]. The mechanism involves a three-layer GB migration normal to the GB plane, during which the upper grain simultaneously shifts by two atomic layers relative to the lower grain. In the pristine Al $\Sigma 5(210)$ STGB, the disconnection nucleation pathway is highly sensitive to the choice of interatomic potential. Shear simulations using some embedded-atom method (EAM) potentials [44,45] reproduce the same shear-coupling factor $\beta = b/h = 2/3$, while others [46–48] predict a different nucleation pathway. This alternative involves a single-layer normal migration and yields a higher shear-coupling factor of $\beta_0 = b_0/h_0 = 4$, with the corresponding path highlighted by the dashed light blue kite in FIG. 2.

In contrast, the orange and red (\mathbf{b}, h) pairs in FIG. 2 demonstrate two potential nucleation pathways for disconnections driven by solute interstitial segregation characterized by the EAM potential for Al-Ni [48]. Notably, both pathways involve single-layer GB migration but result in step heights of equal magnitude and opposite signs: $h_1 = -h_2 = h/3$. The topological locations of the relevant interstitial sites are defined by the intersection points of the short-dashed black lines connecting sites 2–3' and 2'–3 within the kite structures shown in FIG. 2. Topological analysis reveals that both disconnections share the same

Burgers vector: $\mathbf{b}_1 = \mathbf{b}_2 = 2\mathbf{b}/3$. Consequently, their shear-coupling factors are also equal in magnitude but opposite in signs, i.e., $\beta'_1 = -\beta'_2 = 4/3$.

Although the specific nucleation pathway for pristine Al $\Sigma 5(210)$ STGB may vary depending on the selection of interatomic potential, these variations do not affect the occurrence of interstitial segregation or the formation of disconnections in the corresponding binary systems. For instance, hybrid MD/MC simulations using the EAM potential for the Al-Fe system [45] reproduced the same permanent disconnections activated by the interstitial segregation of Fe in Al (FIG. S5 [27]) as those presented in FIG. 1, despite the shear-coupling factor being $2/3$ for the pristine Al $\Sigma 5(210)$ STGB using the Al-Fe EAM potential [45].

The nucleation pathways of interstitial segregation-induced disconnections are confirmed by molecular statics simulations at 0 K (FIG. S4 [27]), which indicate that such disconnections can nucleate without an energy barrier and are solely driven by solute interstitial segregation. Moreover, the estimated shear-coupling factors closely match those predicted by dichromatic pattern analysis (FIG. S4 [27]), reinforcing the distinct nucleation mechanism activated by interstitial segregation.

The segregation-activated disconnections also show distinct kinetics under shear, as demonstrated in FIG. 3 based on bicrystal samples containing pristine, saturated, and saturated/disconnected GBs at 0 K. In the pristine sample, when the shear stress reaches a critical value ($\tau_p^c = 2.02$ GPa), the GB undergoes a shear-coupled motion, accompanied by a sudden drop in shear stress. Upon further displacement, the system enters another elastic loading phase until the shear stress again reaches the critical threshold, prompting repeated shear-coupled migration events [5,49]. FIG. 3(b) presents the GB configuration at a displacement of $d = 4.0$ nm, where the GB has migrated upward, and the kites are visibly distorted. The estimated shear-coupling factor, $\beta_0 = 4.01$, closely matches the value 4.0 obtained from dichromatic pattern analysis in FIG. 2, confirming the reliability of the dichromatic pattern analysis.

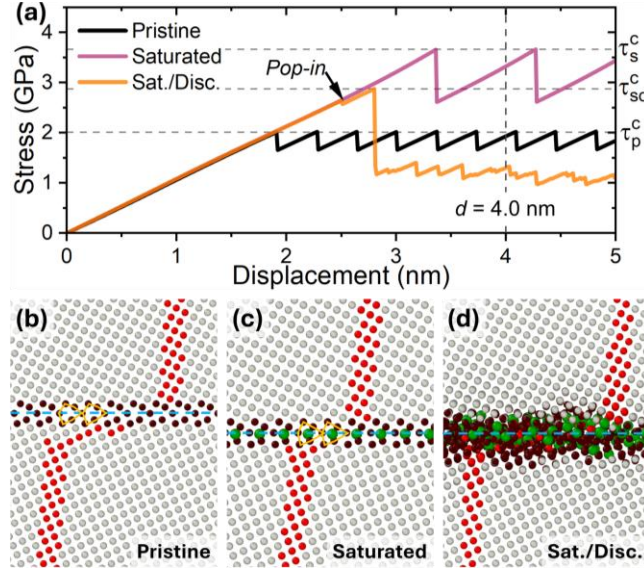


FIG. 3 (a) Shear stress-displacement curves for bicrystals with pristine, saturated, and saturated/disconnected $\Sigma 5(210)$ STGBs. (b)-(d) GB behaviors at the displacement $d = 4.0$ nm. Red spheres serve as markers to track GB behavior under applied shear, while green spheres represent Ni atoms (enlarged for clarity).

In the saturated sample, where all interstitial sites are occupied by Ni atoms, the critical shear stress for GB motion is significantly higher ($\tau_s^c = 3.66$ GPa) than that of the pristine case, as shown in FIG. 3(a). Moreover, the GB exhibits pure sliding without any accompanying normal motion at the critical shear stress, as shown in FIG. 3(c). This sliding behavior can be interpreted as a special disconnection mode, characterized by a finite Burgers vector but zero step height. The corresponding dichromatic pattern analysis is illustrated by the light purple arrow in FIG. 2, where the open circles and square marks denote top and bottom interstitial sites, respectively. Accordingly, the Burgers vector is $\mathbf{b}_3 = 5\mathbf{b}$, which is intrinsically linked to the structural periodicity of the $\Sigma 5(210)$ STGB. This is further supported by the observed elementary sliding distance, which spans approximately two GB kites, as shown in FIG. 3(c).

In the saturated/disconnected case, where all interstitial sites are occupied by Ni atoms and a permanent disconnection dipole is present, the critical shear stress ($\tau_{sd}^c = 2.86$ GPa) is higher than that of the pristine case but lower than that of the saturated case, as shown in FIG. 3(a). Notably, a pop-in event occurs at a lower shear stress ($\tau_{sd}^{pop-in} = 2.63$ GPa). This pop-in corresponds to a partial GB migration of the lower region of the interstitially segregated GB (FIG. S6 [27]). During this process, solute atoms transition from interstitial to substitutional sites, while the vacated interstitial sites become occupied by Al atoms. Following the pop-in event, the shear stress increases linearly with displacement until it reaches the critical point, at which the GB undergoes a sudden amorphization, like the GB structure shown in

FIG. 3(c). This is followed by a transition to pure sliding, characterized by a significantly lower stress level, resulting in a flow-like shear stress–displacement response.

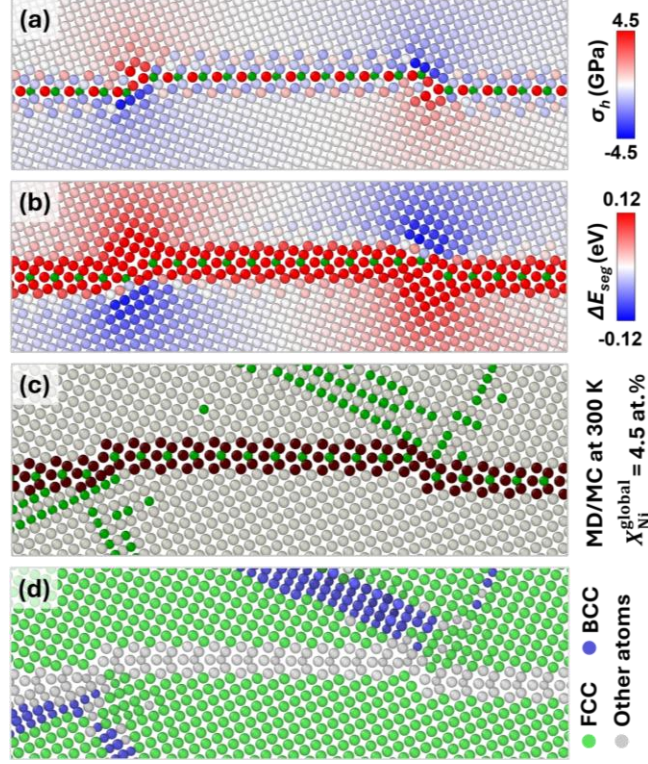


FIG. 4 (a) and (b) are the hydrostatic stress (σ_h) map and the corresponding segregation energy (ΔE_{seg}) map around the permanent disconnection dipole at the Al-Ni $\Sigma 5(210)$ STGBs. (c) Solute distribution at the disconnection dipole after hybrid MD/MC simulations at 300 K with a global solute concentration of 4.5 Ni at.%. (d) Common neighbor analysis of the structures in (c). The green spheres in (a), (b), and (c) represent Ni atoms.

At disconnections, the presence of dislocation components inherently modifies the surrounding stress fields [1], and thereby influencing local segregation patterns [50,51]. As shown in FIG. 4(a), for a given disconnection, the hydrostatic stresses exhibit opposite signs across GB and between its neighbors with opposite Burgers vectors. Here, negative and positive values reveal compressive and tensile regions, respectively. Consistent with the stress distribution, the segregation energy map in FIG. 4(b) mirrors the hydrostatic stress pattern. Compressive regions exhibit favorable segregation, reflected by negative segregation energies, while tensile regions correspond to anti-segregation, with positive segregation energies. This behavior aligns with the known tendency of Ni atoms to preferentially segregate to compressive sites [52].

Once all interstitial sites are occupied by solute atoms, the GB can no longer accommodate additional solute atoms with positive segregation energies, as shown in FIG. 4(b). This behavior indicates the presence of repulsive solute–solute interactions, which stands in stark contrast to the solute–solute

attraction commonly observed in nanocrystalline samples [53]. This discrepancy is likely attributed to the unique structural characteristics induced by interstitial solute segregation. As the solute concentration continues to increase, solute atoms are driven to disconnection cores, leading to local solute enrichment near these regions and promoting the formation of ordered solvent–solute phases (i.e., precipitates), as shown in FIG. 4(c). These precipitates exhibit a body-centered cubic (BCC) structure, as identified by common neighbor analysis shown in FIG. 4(d), indicating they are likely the B2 phase in the Al–Ni system. Composition analysis further confirms this, revealing an approximate Al-to-Ni atomic ratio of 1:1 within the BCC regions, consistent with that of the B2 phase [54].

Besides the Al–Ni and Al–Fe systems, segregation-activated disconnections can also be observed in other face-centered cubic system, such as Al–Cu [55] and BCC systems like Ta–Cu [56], and W–Fe [57] within the $\Sigma 5(310)$ STGBs (FIG. S5 [27]). Additionally, such disconnections were also identified within the $\Sigma 13(320)$ STGB in the Al–Ni system (FIG. S7 [27]). In each of these binary systems, solute atoms preferentially occupy interstitial sites within the center of GB kite structures. In contrast, disconnections are absent in systems where solute atoms only occupy substitutional sites. These findings confirm that the nucleation of unconventional disconnections is activated by GB structural relaxation during which solute atoms segregate to interstitial sites. Furthermore, the interstitial segregation-activated disconnections exhibit a distinct relationship between the shear-coupling factor and GB structures compared to conventional disconnections [1,5], as analyzed in SM [27].

Although interstitial segregation is widely observed in substitutional binary alloys [41], it does not universally lead to disconnection formation. For example, low-angle $\langle 001 \rangle$ STGBs tend to promote precipitation, driven by stress fields from their dislocation array (FIG. S8 [27]). Similarly, $\langle 110 \rangle$ STGBs such as $\Sigma 9(221)$ and $\Sigma 11(332)$ exhibit no such disconnections, as solute interstitials form multi-layered segregation patterns that inhibit disconnection nucleation due to their distinct structures. A comprehensive understanding of solute segregation induced disconnection nucleation across general GBs thus remains an open challenge.

In summary, we report the formation of unconventional GB disconnections induced by solute interstitial segregation in various substitutional binary alloys, including Al–Ni, Al–Fe, Al–Cu, Ta–Cu, and W–Fe, observed from hybrid MD/MC simulations. Unlike conventional GB disconnections, whose nucleation is driven by thermal or mechanical forces, these unconventional disconnections form solely due to solute segregation, follow distinct nucleation pathways, as revealed by dichromatic pattern analysis, and resist

shear, inducing GB amorphization and pure sliding other than conventional shear-coupled motion. The stress fields surrounding segregation-induced disconnections further promote solute accumulation and facilitate the formation of precipitates in specific alloy systems, such as Al–Ni, Al–Fe, and Al–Cu. These findings deepen our understanding of solute-influenced GB kinetics and highlight the need for further investigation into segregation-activated disconnections across broader alloy systems and their potential role in alloy design.

Acknowledgements

This research was supported by the NSERC Discovery Grant (RGPIN-2019-05834), Canada, and the use of computing resources provided by the Digital Research Alliance of Canada. Z.Z. acknowledges financial support from the University of Manitoba Graduate Fellowship (UMGF). During the preparation of this manuscript, the authors used ChatGPT to improve its readability. The authors carefully reviewed and edited the manuscript following the use of this tool and took full responsibility for the content of the publication.

Reference

- [1] J. Han, S. L. Thomas, and D. J. Srolovitz, Grain-boundary kinetics: A unified approach, *Progress in Materials Science* **98**, 386 (2018).
- [2] J. P. Hirth, Dislocations, steps and disconnections at interfaces, *Journal of Physics and Chemistry of Solids* **55**, 985 (1994).
- [3] J. P. Hirth and R. C. Pond, Steps, dislocations and disconnections as interface defects relating to structure and phase transformations, *Acta Materialia* **44**, 4749 (1996).
- [4] J. P. Hirth, R. C. Pond, and J. Lothe, Spacing defects and disconnections in grain boundaries, *Acta Materialia* **55**, 5428 (2007).
- [5] J. W. Cahn, Y. Mishin, and A. Suzuki, Coupling grain boundary motion to shear deformation, *Acta Materialia* **54**, 4953 (2006).
- [6] H. A. Khater, A. Serra, R. C. Pond, and J. P. Hirth, The disconnection mechanism of coupled migration and shear at grain boundaries, *Acta Materialia* **60**, 2007 (2012).
- [7] Q. Zhu, G. Cao, J. Wang, C. Deng, J. Li, Z. Zhang, and S. X. Mao, In situ atomistic observation of disconnection-mediated grain boundary migration, *Nat Commun* **10**, 156 (2019).
- [8] G. S. Rohrer, I. Chesser, A. R. Krause, S. K. Naghibzadeh, Z. Xu, K. Dayal, and E. A. Holm, Grain Boundary Migration in Polycrystals, *Annu. Rev. Mater. Res.* **53**, 347 (2023).
- [9] Y. Deng and C. Deng, Size and rate dependent grain boundary motion mediated by disconnection nucleation, *Acta Materialia* **131**, 400 (2017).
- [10] G. L. Kelley and J. Winlock, On the restraint of exaggerated grain growth in critically strained metal, *Journal of the Franklin Institute* **201**, 71 (1926).
- [11] A. Bhattacharya, Y.-F. Shen, C. M. Hefferan, S. F. Li, J. Lind, R. M. Suter, C. E. Krill, and G. S. Rohrer, Grain boundary velocity and curvature are not correlated in Ni polycrystals, *Science* **374**, 189 (2021).

- [12] J. W. Cahn and J. E. Taylor, A unified approach to motion of grain boundaries, relative tangential translation along grain boundaries, and grain rotation, *Acta Materialia* **52**, 4887 (2004).
- [13] Y. Chen, H. Deng, Q. Zhu, H. Zhou, and J. Wang, Direct observation of disconnection-mediated grain rotation, *Scripta Materialia* **252**, 116279 (2024).
- [14] C. Qiu, M. Salvalaglio, D. J. Srolovitz, and J. Han, Disconnection flow-mediated grain rotation, *Proc. Natl. Acad. Sci. U.S.A.* **121**, e2310302121 (2024).
- [15] Y. Tian et al., Grain rotation mechanisms in nanocrystalline materials: Multiscale observations in Pt thin films, *Science* **386**, 49 (2024).
- [16] L. Zhang, J. Han, Y. Xiang, and D. J. Srolovitz, Equation of Motion for a Grain Boundary, *Phys. Rev. Lett.* **119**, 246101 (2017).
- [17] Y. Chen, J. Han, H. Deng, G. Cao, Z. Zhang, Q. Zhu, H. Zhou, D. J. Srolovitz, and J. Wang, Revealing grain boundary kinetics in three-dimensional space, *Acta Materialia* **268**, 119717 (2024).
- [18] K. Chen, D. J. Srolovitz, and J. Han, Grain-boundary topological phase transitions, *Proc. Natl. Acad. Sci. U.S.A.* **117**, 33077 (2020).
- [19] T. Frolov, M. Asta, and Y. Mishin, Segregation-induced phase transformations in grain boundaries, *Phys. Rev. B* **92**, 020103 (2015).
- [20] Z. Li, P. Zhao, W. Zhang, G. Xie, H. Duan, P. Zeng, S. Ma, J. Zhang, and K. Du, Atomic unveiling of segregation-induced grain boundary structural transition in intermetallic compound, *Acta Materialia* 120830 (2025).
- [21] V. Devulapalli, E. Chen, T. Brink, T. Frolov, and C. H. Liebscher, Topological grain boundary segregation transitions, *Science* **386**, 420 (2024).
- [22] R. W. Balluffi and J. W. Cahn, Mechanism for diffusion induced grain boundary migration, *Acta Metallurgica* **29**, 493 (1981).
- [23] T. Chookajorn, H. A. Murdoch, and C. A. Schuh, Design of Stable Nanocrystalline Alloys, *Science* **337**, 951 (2012).
- [24] M. Hillert, Solute drag, solute trapping and diffusional dissipation of Gibbs energy, *Acta Materialia* **47**, 4481 (1999).
- [25] C. Hu, S. Berbenni, D. L. Medlin, and R. Dingreville, Discontinuous segregation patterning across disconnections, *Acta Materialia* **246**, 118724 (2023).
- [26] C. Hu, D. L. Medlin, and R. Dingreville, Stability and Mobility of Disconnections in Solute Atmospheres: Insights from Interfacial Defect Diagrams, *Phys. Rev. Lett.* **134**, 016202 (2025).
- [27] Supplementary Materials for method details and additional results, which includes Refs. [28-40]., (n.d.).
- [28] S. Plimpton, Fast Parallel Algorithms for Short-Range Molecular Dynamics, *Journal of Computational Physics* **117**, 1 (1995).
- [29] A. Stukowski, Visualization and analysis of atomistic simulation data with OVITO—the Open Visualization Tool, *Modelling Simul. Mater. Sci. Eng.* **18**, 015012 (2009).
- [30] P. M. Larsen, S. Schmidt, and J. Schiøtz, Robust structural identification via polyhedral template matching, *Modelling and Simulation in Materials Science and Engineering* **24**, 055007 (2016).
- [31] B. Sadigh, P. Erhart, A. Stukowski, A. Caro, E. Martinez, and L. Zepeda-Ruiz, Scalable parallel Monte Carlo algorithm for atomistic simulations of precipitation in alloys, *Phys. Rev. B* **85**, 184203 (2012).
- [32] M. A. Tschopp, S. P. Coleman, and D. L. McDowell, Symmetric and asymmetric tilt grain boundary structure and energy in Cu and Al (and transferability to other fcc metals), *Integr Mater Manuf Innov* **4**, 176 (2015).
- [33] N. Metropolis, A. W. Rosenbluth, M. N. Rosenbluth, A. H. Teller, and E. Teller, Equation of State Calculations by Fast Computing Machines, *The Journal of Chemical Physics* **21**, 1087 (1953).

- [34] S. Zhang, O. Y. Kontsevoi, A. J. Freeman, and G. B. Olson, Sodium-induced embrittlement of an aluminum grain boundary, *Phys. Rev. B* **82**, 224107 (2010).
- [35] G. Lu and N. Kioussis, Interaction of vacancies with a grain boundary in aluminum: A first-principles study, *Phys. Rev. B* **64**, 024101 (2001).
- [36] G. Kresse and J. Furthmüller, Efficiency of *ab-initio* total energy calculations for metals and semiconductors using a plane-wave basis set, *Computational Materials Science* **6**, 15 (1996).
- [37] G. Kresse and J. Furthmüller, Efficient iterative schemes for *ab initio* total-energy calculations using a plane-wave basis set, *Phys. Rev. B* **54**, 11169 (1996).
- [38] P. E. Blöchl, Projector augmented-wave method, *Phys. Rev. B* **50**, 17953 (1994).
- [39] J. P. Perdew, K. Burke, and M. Ernzerhof, Generalized Gradient Approximation Made Simple, *Phys. Rev. Lett.* **77**, 3865 (1996).
- [40] D. L. Olmsted, S. M. Foiles, and E. A. Holm, Survey of computed grain boundary properties in face-centered cubic metals: I. Grain boundary energy, *Acta Materialia* **57**, 3694 (2009).
- [41] Z. Zhang and C. Deng, Grain boundary interstitial segregation in substitutional binary alloys, *Acta Materialia* **291**, 121019 (2025).
- [42] I. S. Winter and T. Frolov, Phase Pattern Formation in Grain Boundaries, *Phys. Rev. Lett.* **132**, 186204 (2024).
- [43] Y. Deng and C. Deng, Atomic link between the structure and strength of grain boundaries subject to shear coupling, *Phys. Rev. Materials* **3**, 010601 (2019).
- [44] M. I. Mendelev, M. J. Kramer, C. A. Becker, and M. Asta, Analysis of semi-empirical interatomic potentials appropriate for simulation of crystalline and liquid Al and Cu, *Philosophical Magazine* **88**, 1723 (2008).
- [45] M. I. Mendelev, D. J. Srolovitz, G. J. Ackland, and S. Han, Effect of Fe Segregation on the Migration of a Non-Symmetric $\Sigma 5$ Tilt Grain Boundary in Al, *J. Mater. Res.* **20**, 208 (2005).
- [46] R. R. Zope and Y. Mishin, Interatomic potentials for atomistic simulations of the Ti-Al system, *Phys. Rev. B* **68**, 024102 (2003).
- [47] Y. Mishin, D. Farkas, M. J. Mehl, and D. A. Papaconstantopoulos, Interatomic potentials for monoatomic metals from experimental data and *ab initio* calculations, *Phys. Rev. B* **59**, 3393 (1999).
- [48] G. P. Purja Pun and Y. Mishin, Development of an interatomic potential for the Ni-Al system, *Philosophical Magazine* **89**, 3245 (2009).
- [49] A. Rajabzadeh, F. Momprou, M. Legros, and N. Combe, Elementary Mechanisms of Shear-Coupled Grain Boundary Migration, *Phys. Rev. Lett.* **110**, 265507 (2013).
- [50] C. Hu, S. Berbenni, D. L. Medlin, and R. Dingreville, Discontinuous segregation patterning across disconnections, *Acta Materialia* **246**, 118724 (2023).
- [51] C. Hu, D. L. Medlin, and R. Dingreville, Stability and Mobility of Disconnections in Solute Atmospheres: Insights from Interfacial Defect Diagrams, *Phys. Rev. Lett.* **134**, 016202 (2025).
- [52] Z. Zhang and C. Deng, Hydrostatic pressure-induced transition in grain boundary segregation tendency in nanocrystalline metals, *Scripta Materialia* **234**, 115576 (2023).
- [53] Z. Zhang and C. Deng, Grain boundary segregation prediction with a dual-solute model, *Phys. Rev. Materials* **8**, 103605 (2024).
- [54] M. Settem, On the structural analysis of ordered B2 AlNi nanoparticles obtained using freezing simulations, *Intermetallics* **106**, 115 (2019).
- [55] K. Song et al., General-purpose machine-learned potential for 16 elemental metals and their alloys, *Nat Commun* **15**, 10208 (2024).
- [56] G. P. Purja Pun, K. A. Darling, L. J. Kecskes, and Y. Mishin, Angular-dependent interatomic potential for the Cu-Ta system and its application to structural stability of nano-crystalline alloys, *Acta Materialia* **100**, 377 (2015).

- [57] G. Bonny, N. Castin, J. Bullens, A. Bakaev, T. C. P. Klaver, and D. Terentyev, On the mobility of vacancy clusters in reduced activation steels: an atomistic study in the Fe–Cr–W model alloy, *J. Phys.: Condens. Matter* **25**, 315401 (2013).

Supplementary Materials for
Solute Segregation Activates Unconventional Grain Boundary Disconnections

Zuoyong Zhang and Chuang Deng*

Department of Mechanical Engineering, University of Manitoba, Winnipeg, Manitoba R3T 5V6, Canada

*Contact author: chuang.deng@umanitoba.ca

Methods

Atomistic simulations—The atomistic simulations were conducted using the LAMMPS package [1]. OVITO was used for visualization [2], and the common neighbor analysis (a-CNA) method [3] was employed to analyze atomic structures. Hybrid molecular dynamics (MD)/Monte Carlo (MC) simulations were performed using the variance-constrained semi-grand-canonical (VC-SGC) ensemble [4] to sample the Al bicrystals with symmetry-tilt grain boundaries (STGBs) [5] at 300 K and zero-pressure conditions in the Al-Ni system. Interatomic interactions were modeled using an embedded atom method (EAM) potential [6].

Details of the hybrid MD/MC simulation procedure can be found in our previous studies [7,8]. In this work, we gradually increased the solute concentration in increments of 0.05 at.%. The Al-Ni system was selected as a representative substitutional alloy because hybrid MD/MC sampling at 300 K revealed notable interstitial segregation, accompanied by structural transitions and GB evolution in some coincidence-site lattice (CSL) GBs [7]. These observations led us to hypothesize that interstitial segregation in substitutional alloys may promote the nucleation of disconnections. For alloy systems lacking suitable EAM potentials, we employed the Metropolis algorithm [9] to perform the hybrid MD/MC simulations.

Segregation energy calculations—To evaluate the site occupancy preference, the segregation energy (ΔE_{seg}) of Ni in Al is calculated by substituting a single Ni atom at each solvent site at 0 K under zero-pressure conditions, with periodic boundary conditions applied in all directions, following the approach described in Ref. [10]. This single-solute substitution method can avoid local structure transitions at GBs during energy minimization.

Shear deformation—Following the method described in Ref. [11], shear simulations were performed at 0 K by applying incremental shear displacements to the top and bottom slabs in opposite directions (along x -axis), parallel to the GB plane. After each increment, the system energy was minimized using the conjugate gradient method. Periodic boundary conditions are applied along x - and z -directions, while leaving y -direction as free. The simulation cell layout and initial GB configurations of the samples are shown in FIG. S1.

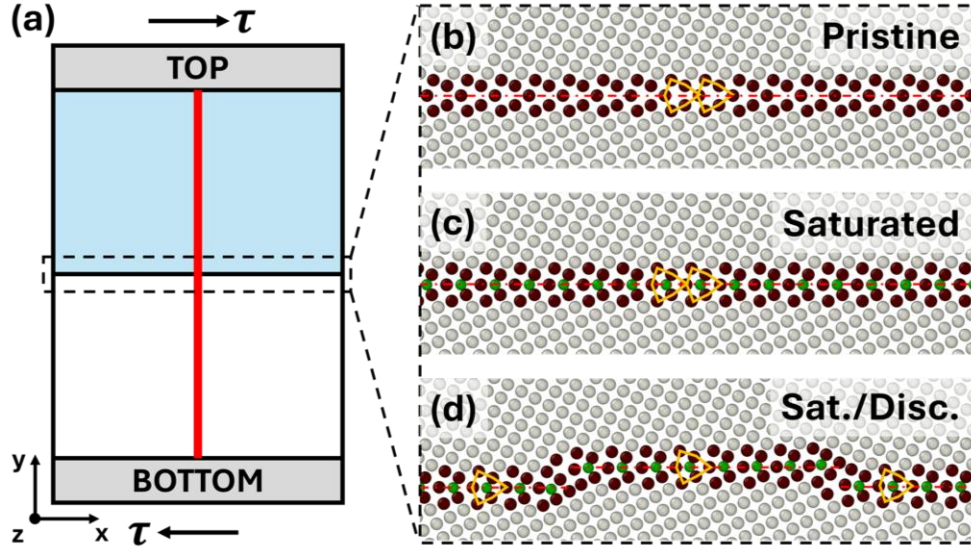


FIG. S1 (a) Schematic illustration of shear displacement simulation cell. (b)-(d) Initial grain boundary (GB) configurations for the (b) pristine, (c) saturated, and (d) saturated/disconnected (sat./disc.) samples. Grey spheres represent bulk Al atoms, dark brown spheres indicate Al atoms at the GBs, and green spheres denote Ni atoms.

GB excess energy calculations—Molecular statics (MS) simulations were performed to calculate the GB excess energy (γ_{GB}) for the pure and segregated $\Sigma 5(210)$ STGBs using the Eq. (S1):

$$\gamma_{GB} = \frac{E_{GB} - E_{bulk}}{2A}, \quad (1)$$

where E_{GB} is the system energy with two GBs, while E_{bulk} refers to the total potential energy of the equivalent bulk system. A is the area of GB plane in the simulation cell. The resulting γ_{GB} for the pristine Al $\Sigma 5(210)$ STGB is 0.494 J/m^2 , consistent with the first-principles results 0.501 J/m^2 [12] and 0.502 J/m^2 [13], as shown in FIG. S2(a), indicating the reliability of this MS method. FIG. S2(a) also shows that γ_{GB} linearly reduces with solute concentration in the Al-Ni system. FIG. S2(b) shows that increasing

disconnection density can significantly increase the GB excess energy, offering a negative effect to the reduction in γ_{GB} .

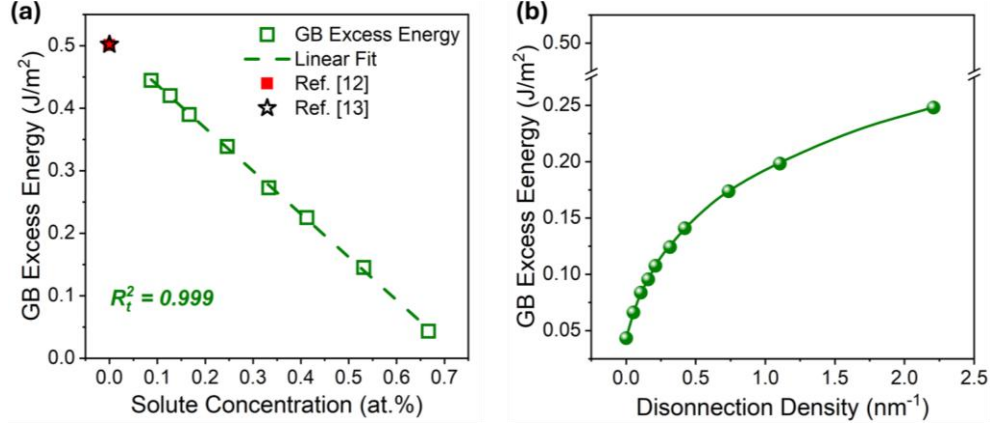


FIG. S2 (a) GB excess energy as a function of solute concentration for the Al-Ni system with $\Sigma 5(210)$ STGB. The red filled square and black open star are GB excess energy from first-principles results [12,13]. (b) GB excess energy as a function of permanent disconnection density.

First-principles simulations—First-principles simulations were performed using the Vienna Ab-initio Simulation Package (VASP) [14,15], employing the projector augmented-wave (PAW) method [16]. The exchange–correlation potential was treated using the generalized gradient approximation (GGA) in the Perdew–Burke–Ernzerhof (PBE) form [17]. A cutoff energy of 400 eV and a Monkhorst–Pack k-point mesh of $6 \times 6 \times 4$ were used. The convergence criteria were set to 10^{-6} eV for total energy and 10^{-2} eV/Å for atomic forces during the relaxation. The $\Sigma 5(210)$ STGB in Al was constructed following the method described in Ref. [18]. The initial bicrystal model, consisting of 160 Al atoms, was first relaxed (FIG. S2(a)). Subsequently, the 3 or 3' sites (FIG. S3(b) and (d)) were substituted with solute atoms (Ni, Fe, or Cu), followed by additional full relaxation to obtain the final configuration (FIG. S3(c) and (e)). Permanent disconnections formed after full relaxation as described in the main text.

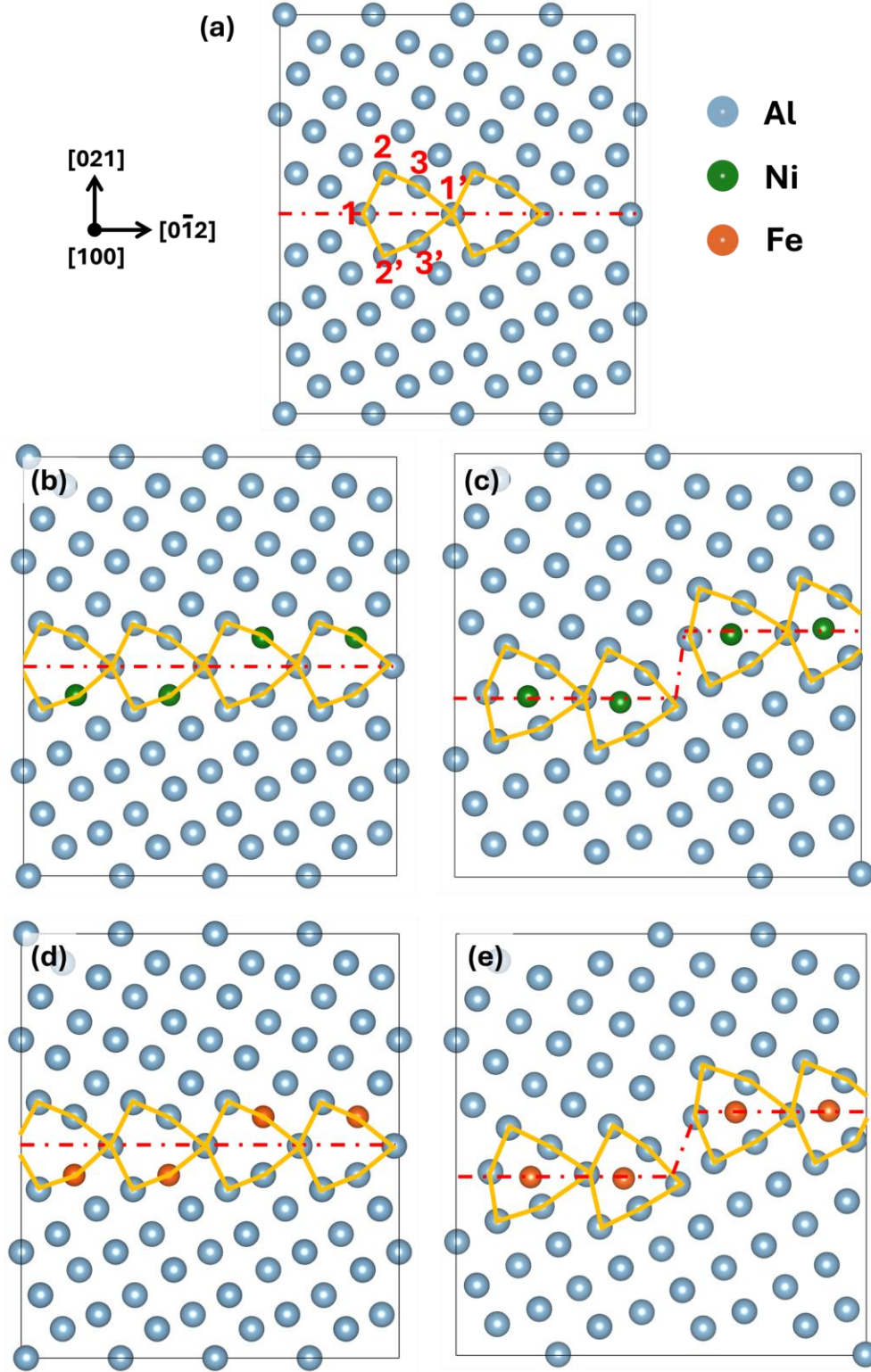


FIG. S3 (a) Fully relaxed Al $\Sigma 5(210)$ STGB bicrystal. (b) and (d) Substitute 3 or 3' sites with solute atoms (Ni and Fe). (c) and (e) Final GB structures after full relaxation.

Estimation of Burgers vector—MS simulations were performed to estimate the magnitude of the Burgers vector associated with interstitial segregation–activated GB migration in a $\Sigma 5(210)$ STGB, using the Al–Ni system as a representative case. Following the procedure used in the first-principles simulations, Ni atoms were substituted at the 3 (FIG. S4(a)) and 3' (FIG. S4(c)) sites. The bicrystal structure was then relaxed using the conjugate gradient algorithm. During relaxation, the upper and lower layers near GB were used as markers. The Burgers vector \mathbf{b} and step height h were estimated based on the displacement of the mass centers of these two marker regions. The measured values for downward migration are: $b_1 = 0.95 \text{ \AA}$ and $h_1 = -0.75 \text{ \AA}$, where the minus sign in h_1 refers to the downward displacement. Therefore, the resulting shear-coupling factor is $\beta_1 = -1.27$, which matches the dichromatic pattern analysis value of $-4/3$ in the main text. As for the upward scenario (FIG. S4(c) and (d)), the measured values are: $b_2 = 0.95 \text{ \AA}$ and $h_2 = 0.75 \text{ \AA}$, and the resulting shear-coupling factor ($\beta_2 = 1.27$) also matches the dichromatic pattern analysis value of $4/3$.

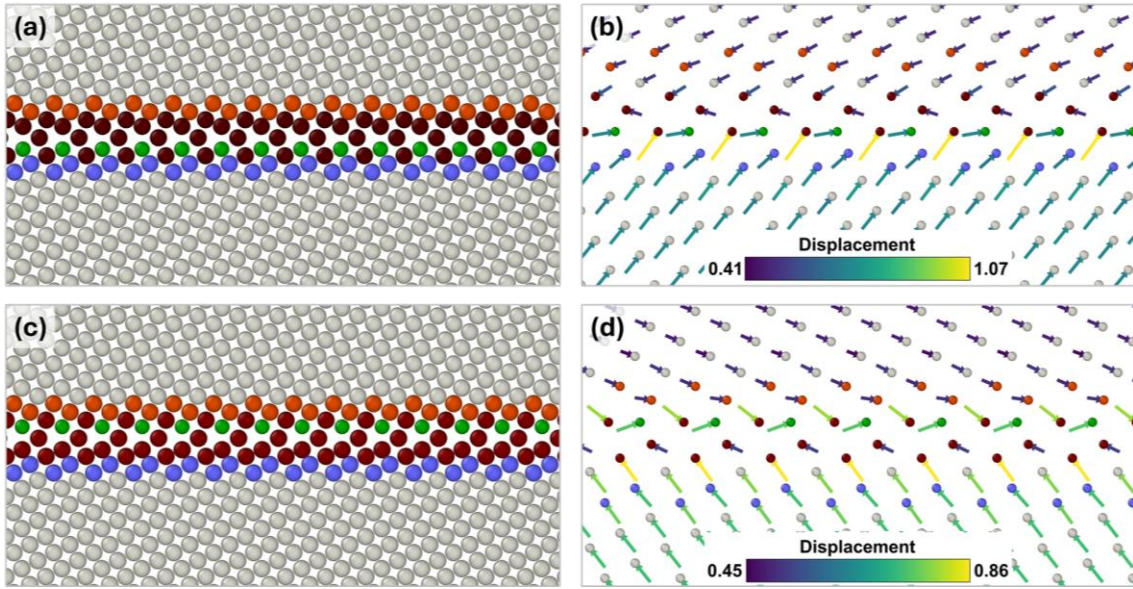


FIG. S4 (a) and (c) Initial GB structures used to measure Burgers vectors for downward and upward migrations, respectively, in the Al–Ni system with a $\Sigma 5(210)$ STGB. Red and blue spheres indicate the upper and lower marker layers, respectively. (b) and (d) Corresponding atomic displacements during MS simulations for configurations (a) and (c), respectively. A scaling factor of 2 was applied to the displacement vectors for improved visualization.

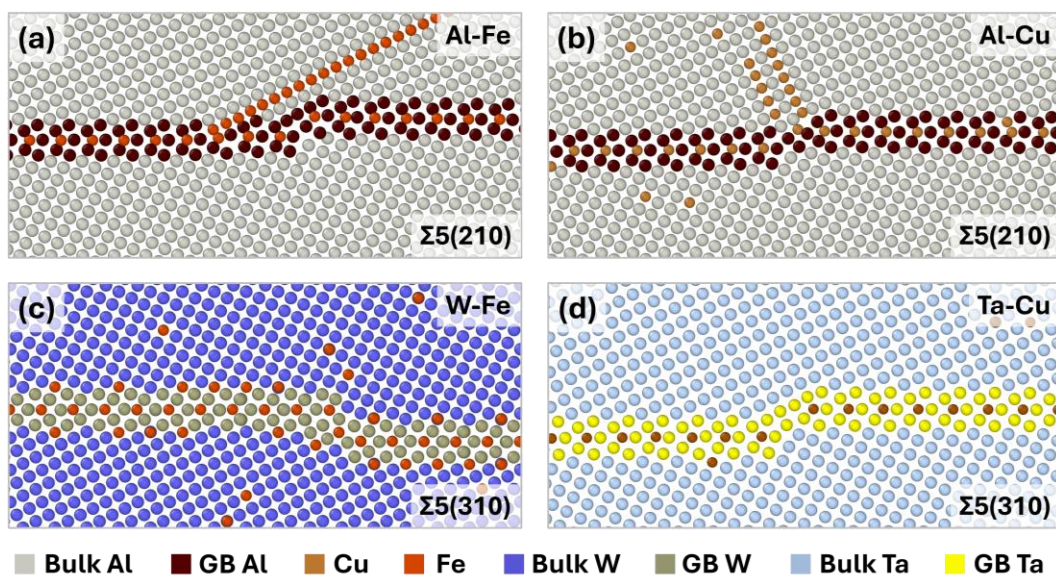


FIG. S5 Permanent disconnections in the (a) Al-Fe, (b) Al-Cu, (c) W-Fe, and (d) Ta-Cu formed during the hybrid MD/MC simulations. Ordered solvent-solute structures (precipitates) can be observed in the Al-Fe and Al-Cu systems.

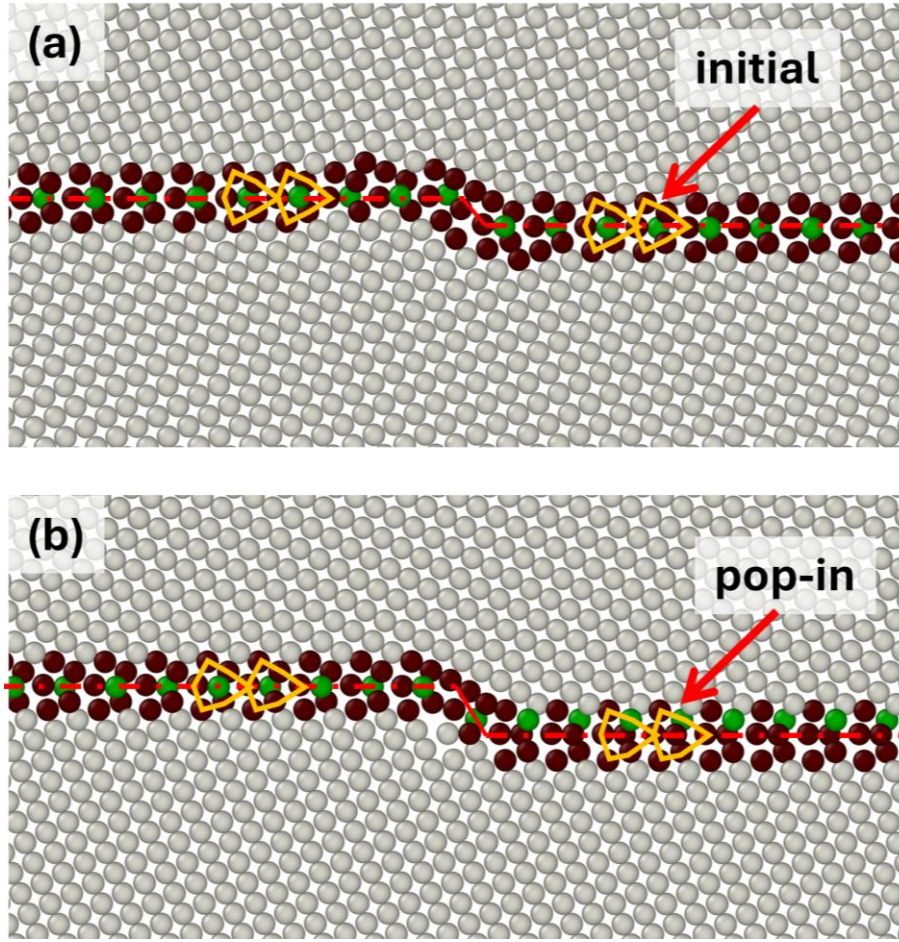


FIG. S6 (a) Initial GB structure of the Sat./Disc. scenario when shear displacement $d = 0$ nm. (b) Deformed GB structure when shear displacement $d = 2.5$ nm, where part of the kite structures has a one-layer downward migration.

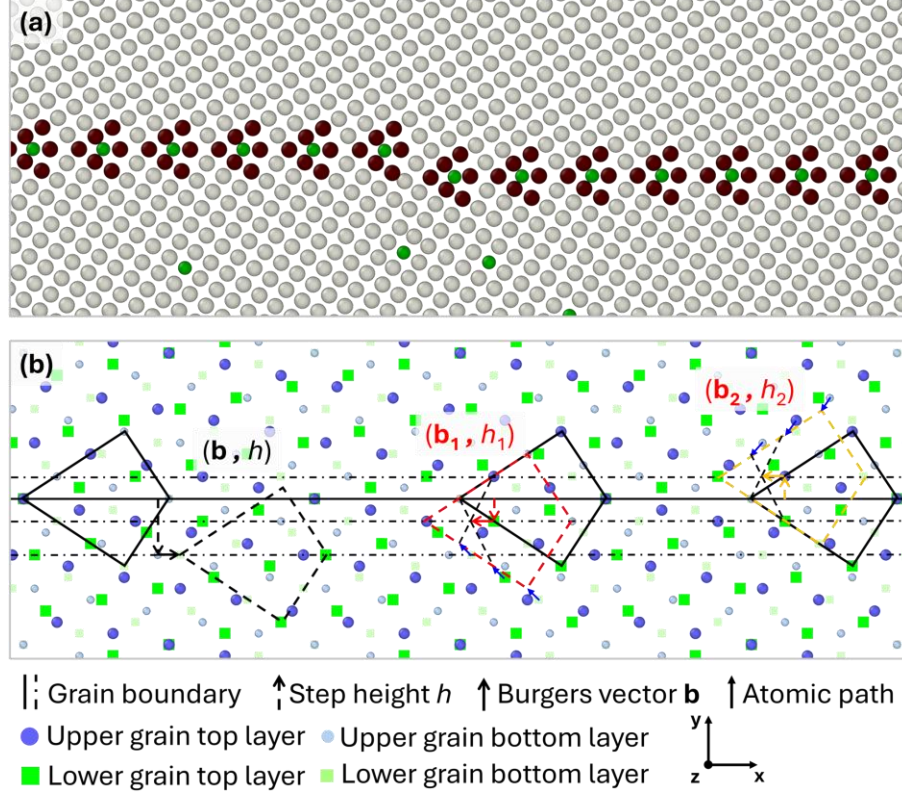


FIG. S7 (a) Permanent disconnection formed after hybrid MD/MC simulations in the $\Sigma 13(320)$ STGB of the Al-Ni system. (b) Dichromatic pattern analysis of the disconnection nucleation paths in the $\Sigma 13(320)$ STGB. The black dashed kite with (b, h) pair indicates the disconnection nucleation path for pristine $\Sigma 13(320)$ STGB, whose shear coupling factor $\beta = b/h = -0.4$ [19]. However, the shear coupling factors for segregation activated disconnection are $\beta_1 = -\beta_2 = 1$.

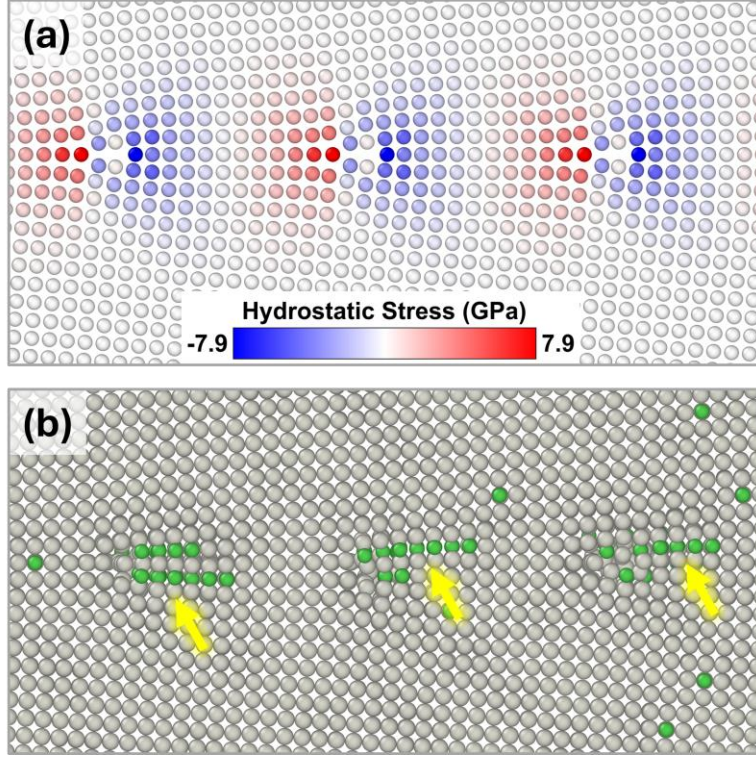


FIG. S8 (a) Hydrostatic stress maps for the $\langle 001 \rangle$ (14 1 0) STGB in Ref. [5]. (b) Corresponding GB structure after hybrid MD/MC simulations at 300 K with the solute concentration of 1 at.%. Apparently, Ni atoms tend to accumulate at the compressive regions and form ordered Al-Ni precipitates, as highlighted by the light-yellow arrows.

Disconnection nucleation criterion analysis—In pristine GBs, conventional disconnections nucleate in $\langle 100 \rangle$ or $\langle 110 \rangle$ modes depending on the corresponding Burgers vector direction, and resulting in the following nucleation criteria [19]:

$$b_{\langle 100 \rangle} = a \sin(\theta/2), \quad (2)$$

$$h_{\langle 100 \rangle} = (a/2) \cos(\theta/2), \quad (3)$$

$$\beta_{\langle 100 \rangle} = 2 \tan(\theta/2), \quad (4)$$

and

$$b_{\langle 110 \rangle} = \sqrt{2}a \sin(\varphi/2), \quad (5)$$

$$h_{\langle 110 \rangle} = -\sqrt{2}a \cos(\varphi/2), \quad (6)$$

$$\beta_{\langle 110 \rangle} = -2 \tan(\varphi/2), \quad (7)$$

where θ is the tilt angle of the GB, a is the lattice constant for the pure system, and φ is the complement angle for θ : $\varphi = 90^\circ - \theta$.

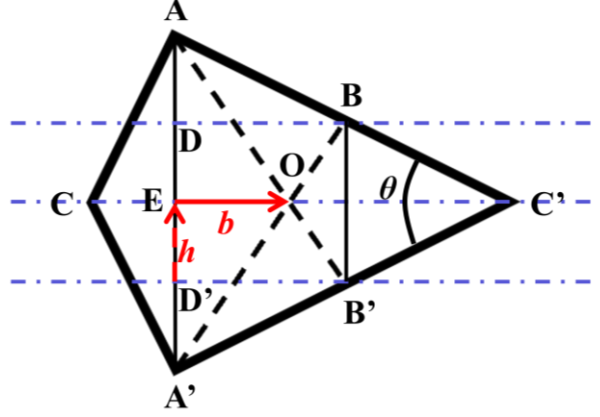


FIG. S9 Schematic illustration of the nucleation path for a segregation activated disconnection.

Nevertheless, the nucleation pathways for solute segregation-activated disconnections are markedly different from those in pristine tilt GBs, and the corresponding nucleation criteria also differ. To analyze these criteria, we begin with a topological examination of the kite structure in a $\Sigma 5(210)$ STGB. As shown in FIG. S9, points B and B' are located at the centers of the kite structure and correspond to the midpoints of segments A-C' and A'-C', respectively, with each segment having a length equal to the lattice constant a . The vertical distance between points A and A' is always twice the horizontal distance between points B and B', i.e., $AA' \equiv 2BB'$. Therefore,

$$b = (a/3) \cos(\theta/2), \quad (8)$$

$$h = (a/2) \sin(\theta/2), \quad (9)$$

$$\beta = b/h = (2/3) \cot(\theta/2), \quad (10)$$

Eqs. (8)–(10) differ significantly from those in pristine cases. Notably, the direction of the Burgers vectors in segregation-activated disconnections always aligns with the orientation of the kite structure, specifically, along the C-C' direction, as illustrated in FIG. S9. Therefore, the sign of β depends on the migration direction and kite orientation.

Reference

- [1] S. Plimpton, Fast Parallel Algorithms for Short-Range Molecular Dynamics, *Journal of Computational Physics* 117 (1995) 1–19. <https://doi.org/10.1006/jcph.1995.1039>.
- [2] A. Stukowski, Visualization and analysis of atomistic simulation data with OVITO—the Open Visualization Tool, *Modelling Simul. Mater. Sci. Eng.* 18 (2009) 015012. <https://doi.org/10.1088/0965-0393/18/1/015012>.
- [3] P.M. Larsen, S. Schmidt, J. Schiøtz, Robust structural identification via polyhedral template matching, *Modelling and Simulation in Materials Science and Engineering* 24 (2016) 055007.
- [4] B. Sadigh, P. Erhart, A. Stukowski, A. Caro, E. Martinez, L. Zepeda-Ruiz, Scalable parallel Monte Carlo algorithm for atomistic simulations of precipitation in alloys, *Phys. Rev. B* 85 (2012) 184203. <https://doi.org/10.1103/PhysRevB.85.184203>.
- [5] M.A. Tschopp, S.P. Coleman, D.L. McDowell, Symmetric and asymmetric tilt grain boundary structure and energy in Cu and Al (and transferability to other fcc metals), *Integr Mater Manuf Innov* 4 (2015) 176–189. <https://doi.org/10.1186/s40192-015-0040-1>.
- [6] G.P. Purja Pun, Y. Mishin, Development of an interatomic potential for the Ni-Al system, *Philosophical Magazine* 89 (2009) 3245–3267. <https://doi.org/10.1080/14786430903258184>.
- [7] Z. Zhang, C. Deng, Grain boundary interstitial segregation in substitutional binary alloys, *Acta Materialia* 291 (2025) 121019. <https://doi.org/10.1016/j.actamat.2025.121019>.
- [8] Z. Zhang, C. Deng, Grain boundary segregation prediction with a dual-solute model, *Phys. Rev. Materials* 8 (2024) 103605. <https://doi.org/10.1103/PhysRevMaterials.8.103605>.
- [9] N. Metropolis, A.W. Rosenbluth, M.N. Rosenbluth, A.H. Teller, E. Teller, Equation of State Calculations by Fast Computing Machines, *The Journal of Chemical Physics* 21 (1953) 1087–1092. <https://doi.org/10.1063/1.1699114>.
- [10] Z. Zhang, C. Deng, Hydrostatic pressure-induced transition in grain boundary segregation tendency in nanocrystalline metals, *Scripta Materialia* 234 (2023) 115576. <https://doi.org/10.1016/j.scriptamat.2023.115576>.
- [11] A. Rajabzadeh, F. Momprou, M. Legros, N. Combe, Elementary Mechanisms of Shear-Coupled Grain Boundary Migration, *Phys. Rev. Lett.* 110 (2013) 265507. <https://doi.org/10.1103/PhysRevLett.110.265507>.
- [12] S. Zhang, O.Y. Kontsevoi, A.J. Freeman, G.B. Olson, Sodium-induced embrittlement of an aluminum grain boundary, *Phys. Rev. B* 82 (2010) 224107. <https://doi.org/10.1103/PhysRevB.82.224107>.
- [13] G. Lu, N. Kioussis, Interaction of vacancies with a grain boundary in aluminum: A first-principles study, *Phys. Rev. B* 64 (2001) 024101. <https://doi.org/10.1103/PhysRevB.64.024101>.

- [14] G. Kresse, J. Furthmüller, Efficiency of ab-initio total energy calculations for metals and semiconductors using a plane-wave basis set, Computational Materials Science 6 (1996) 15–50. [https://doi.org/10.1016/0927-0256\(96\)00008-0](https://doi.org/10.1016/0927-0256(96)00008-0).
- [15] G. Kresse, J. Furthmüller, Efficient iterative schemes for *ab initio* total-energy calculations using a plane-wave basis set, Phys. Rev. B 54 (1996) 11169–11186. <https://doi.org/10.1103/PhysRevB.54.11169>.
- [16] P.E. Blöchl, Projector augmented-wave method, Phys. Rev. B 50 (1994) 17953–17979. <https://doi.org/10.1103/PhysRevB.50.17953>.
- [17] J.P. Perdew, K. Burke, M. Ernzerhof, Generalized Gradient Approximation Made Simple, Phys. Rev. Lett. 77 (1996) 3865–3868. <https://doi.org/10.1103/PhysRevLett.77.3865>.
- [18] D.L. Olmsted, S.M. Foiles, E.A. Holm, Survey of computed grain boundary properties in face-centered cubic metals: I. Grain boundary energy, Acta Materialia 57 (2009) 3694–3703. <https://doi.org/10.1016/j.actamat.2009.04.007>.
- [19] J.W. Cahn, Y. Mishin, A. Suzuki, Coupling grain boundary motion to shear deformation, Acta Materialia 54 (2006) 4953–4975. <https://doi.org/10.1016/j.actamat.2006.08.004>.